Assessment of the ghost fluid method for sharp-interface multiphase flow simulations

By H. Hwang

We revisit the ghost fluid method (GFM) formulation and evaluate its performance through a series of canonical test cases, including a static drop, a damped surface wave, and a two-phase shear layer. The GFM employs a sharp Heaviside function for the discretization of surface tension force and explicitly enforces interfacial jump conditions without relying on smeared interface representations. The results demonstrate that, when coupled with the height function for curvature calculation, the GFM achieves second-order convergence in curvature estimation and accurately reproduces the pressure jump, indicating a significant reduction in spurious currents compared to several popular continuum surface force (CSF) approaches that rely on diffuse-interface representation. The method also exhibits superior agreement with analytical solutions for moving interface problems even at coarse grid resolutions. In the shear layer test, the current implementation remains unaffected by the diffused phase indicator function, unlike the compared CSF approaches, which suffer from degraded accuracy in the heavy-fluid region.

1. Introduction

Capturing sharp interfaces in multiphase flow simulations has drawn increasing attention due to their ubiquity in natural phenomena and engineering applications. Beyond achieving robust and accurate interface representation, the parallelization efficiency of the numerical algorithm on exascale machines has become a crucial factor in developing two-phase flow solvers. In this context, substantial progress has been made on algebraic Volume-of-Fluid (VOF) methods, which arguably lend themselves better to parallelization than geometric VOF approaches by mitigating localized workload imbalance, although this point remains debated. More recently, diffuse-interface methods have gained popularity for their simplicity and excellent parallel scalability in complex multiphase flows (Hwang & Jain 2024). These approaches model the interface as a finite transition region where fluid properties vary smoothly, rather than as a truly sharp discontinuity. In such schemes, the phase indicator extends over a finite number of grid cells, and surface tension is commonly modeled using CSF methods because they offer computational simplicity and acceptable accuracy (Brackbill *et al.* 1992).

While these techniques have successfully predicted complex interfacial flows, special consideration must be given to ensuring a well-balanced formulation and accurate curvature calculation at the interface in order to achieve reliable results. Without such careful treatment, these methods may still suffer from spurious currents and numerical artifacts, particularly when the interface is under-resolved and its characteristic thickness becomes comparable to the relevant physical length scales. Furthermore, maintaining a well-defined material interface remains a significant challenge for finite-thickness representations. For example, artificial sharpening terms introduced to control interface thickness often impose additional constraints on numerical stability and parallel efficiency.

The GFM was originally developed to overcome the numerical smearing inherent to

delta-function-based immersed boundary methods (Peskin 1977). First introduced by Fedkiw *et al.* (1999) for the inviscid Euler equations, the GFM treats the material discontinuities directly within the discretization operators. The method implicitly represents the interface and introduces ghost cells to transform a complex multimaterial problem into a single-material formulation. Kang *et al.* (2000) extended the GFM to incompressible flows including viscosity, surface tension, and gravity, demonstrating promising results for flows with large density ratios. Although the GFM was originally developed with the level-set (LS) method, it has since been coupled with VOF formulations. For instance, Sussman *et al.* (2007) combined LS and VOF techniques to achieve accurate solutions on relatively coarse grids, while Desjardins *et al.* (2008) implemented the GFM with a conservative LS method and emphasized its advantages for high-density-ratio flows and parallel efficiency. Similarly, Bo & Grove (2014) applied the GFM in conjunction with a VOF method for compressible multiphase flows.

Applications of the GFM have been explored across a wide range of configurations—from solving Euler equations on structured Cartesian grids using the LS framework to more complex unstructured meshes that incorporate additional forces. Vukčević *et al.* (2017) investigated the discretization of gravity terms in a GFM–VOF framework on unstructured grids, while Lalanne *et al.* (2015) provided a comprehensive comparison of the viscous discretizations proposed by Kang *et al.* (2000) and Sussman *et al.* (2007). More recently, Peltonen *et al.* (2020) compared two-phase and single-phase GFM formulations, finding moderate advantages of the GFM but no decisive superiority. Cho & Kang (2021) further improved the approach by extrapolating interfacial velocities to nearby grid points, enabling more accurate enforcement of jump conditions in viscosity and pressure through an iterative correction procedure.

In this study, we revisit the derivation of the GFM and systematically evaluate its applicability through a series of canonical test cases. Our objective is to identify the flow conditions and numerical configurations under which the GFM provides clear benefits—particularly for flows characterized by strong shear or requiring the resolution of fine-scale interfacial features. It is important to note that, although the GFM can be applied to various flow regimes, this study focuses exclusively on incompressible, immiscible flows without phase change.

2. Methodology

2.1. *Governing equations*

We consider incompressible, immiscible two-phase flows with viscosity, surface tension, and gravity within a computational domain Ω. The domain Ω composed of two fluids, Ω_+ and Ω_- ($\Omega_+ \cup \Omega_- = \Omega$), with a interface Γ. The governing equation is given by

$$\rho\left(\frac{\partial \mathbf{u}}{\partial t} + \mathbf{u}\cdot\nabla\mathbf{u}\right) = \nabla\cdot\left[\mu\left(\nabla\mathbf{u} + (\nabla\mathbf{u})^{\mathrm{T}}\right)\right] - \nabla p + \rho\mathbf{g} + \gamma\kappa\mathbf{n}\delta_\Gamma, \tag{2.1}$$

subject to the incompressibility constraint $\nabla\cdot\mathbf{u} = 0$. Here, $\mathbf{u}$ is the velocity vector, and ρ, μ, and p denote the density, viscosity, and pressure, respectively, while $\mathbf{g}$ represents gravitational acceleration. The terms γ, κ, $\mathbf{n}$, and δ_Γ correspond to the surface tension coefficient, interface curvature, interface normal vector, and Dirac delta function localized at the interface.

To simplify the treatment of the gravitational term and well-balanced approach, we

define the pseudo-dynamic pressure

$$p_d = p - \rho(\mathbf{g}\cdot\mathbf{x}), \tag{2.2}$$

so that Eq. (2.1) becomes

$$\rho\left(\frac{\partial \mathbf{u}}{\partial t} + \mathbf{u}\cdot\nabla\mathbf{u}\right) = \nabla\cdot\left[\mu\left(\nabla\mathbf{u} + (\nabla\mathbf{u})^{\mathrm{T}}\right)\right] - \nabla p_d - \nabla\rho(\mathbf{g}\cdot\mathbf{x}) + \gamma\kappa\mathbf{n}\delta_\Gamma. \tag{2.3}$$

For a piecewise-constant density field, the density gradient is given by $\nabla\rho = [\rho]_\Gamma\,\mathbf{n}\delta_\Gamma$, where $[\cdot]_\Gamma = (\cdot)_+ - (\cdot)_-$ denotes the jump across the interface Γ. Substituting this relation into Eq. (2.3) yields a jump-condition formulation of the flow equations,

$$\rho\left(\frac{\partial \mathbf{u}}{\partial t} + \mathbf{u}\cdot\nabla\mathbf{u}\right) = \nabla\cdot\left[\mu\left(\nabla\mathbf{u} + (\nabla\mathbf{u})^{\mathrm{T}}\right)\right] - \nabla p_d, \tag{2.4}$$

$$\nabla\cdot\mathbf{u} = 0, \tag{2.5}$$

subject to the interfacial jump conditions

$$[\mathbf{u}] = 0, \tag{2.6}$$

$$[\boldsymbol{\sigma}\mathbf{n}] = \mathbf{G}, \tag{2.7}$$

where $\boldsymbol{\sigma} = \mu\left(\nabla\mathbf{u} + (\nabla\mathbf{u})^{\mathrm{T}}\right) - p_d\mathbf{I}$ is the stress tensor and $\mathbf{G} = (\gamma\kappa - [\rho]_\Gamma\,\mathbf{g}\cdot\mathbf{x})\mathbf{n}$ represents the net interfacial force.

2.2. *Derivation of jump conditions*

Let $\boldsymbol{\tau}_1$, $\boldsymbol{\tau}_2$ denote two orthogonal tangential vectors along the interface. The jump conditions in Eq. (2.7) can be projected along the tangential and normal directions to decompose the stress balance (Cho & Kang 2021).

First, taking the tangential projection of Eq. (2.7) gives

$$\begin{aligned}\mathbf{G}\cdot\boldsymbol{\tau}_i &= [\mu\left(\boldsymbol{\tau}_i\cdot\nabla\mathbf{u}\cdot\mathbf{n} + \mathbf{n}\cdot\nabla\mathbf{u}\cdot\boldsymbol{\tau}_i\right)] \\ &= \boldsymbol{\tau}_i\cdot\left[\mu\frac{\partial\mathbf{u}}{\partial\mathbf{n}}\right] + \mathbf{n}\cdot\left[\mu\frac{\partial\mathbf{u}}{\partial\boldsymbol{\tau}_i}\right],\end{aligned} \tag{2.8}$$

and by the rotational invariance of the divergence (Cho & Kang 2021),

$$\mathbf{n}\cdot\left[\mu\frac{\partial\mathbf{u}}{\partial\mathbf{n}}\right] + \boldsymbol{\tau}_1\cdot\left[\mu\frac{\partial\mathbf{u}}{\partial\boldsymbol{\tau}_1}\right] + \boldsymbol{\tau}_2\cdot\left[\mu\frac{\partial\mathbf{u}}{\partial\boldsymbol{\tau}_2}\right] = 0. \tag{2.9}$$

By combining Eqs. (2.8) and (2.9), the viscous jump condition can be expressed compactly as

$$\begin{aligned}[\mu\nabla\mathbf{u}] = &\left(\mathbf{N}_1\begin{pmatrix}\left[\mu\frac{\partial\mathbf{u}}{\partial\boldsymbol{\tau}_1}\right] & 0 & 0\end{pmatrix} + \mathbf{N}_2\begin{pmatrix}\left[\mu\frac{\partial\mathbf{u}}{\partial\boldsymbol{\tau}_2}\right] & 0 & 0\end{pmatrix}\right. \\ &\left. + \begin{pmatrix}0 & \left[\mu\frac{\partial\mathbf{u}}{\partial\boldsymbol{\tau}_1}\right] & \left[\mu\frac{\partial\mathbf{u}}{\partial\boldsymbol{\tau}_2}\right]\end{pmatrix} + (\mathbf{N}_c \quad 0 \quad 0)\right)(\mathbf{n} \quad \boldsymbol{\tau}_1 \quad \boldsymbol{\tau}_2)^T,\end{aligned} \tag{2.10}$$

where

$$\mathbf{N}_1 = (\mathbf{n} \quad \boldsymbol{\tau}_1 \quad \boldsymbol{\tau}_2)(\boldsymbol{\tau}_1 \quad \mathbf{n} \quad 0)^T, \tag{2.11}$$

$$\mathbf{N}_2 = -(\mathbf{n} \quad \boldsymbol{\tau}_1 \quad \boldsymbol{\tau}_2)(\boldsymbol{\tau}_2 \quad 0 \quad \mathbf{n})^T, \tag{2.12}$$

$$\mathbf{N}_c = (\mathbf{n} \quad \boldsymbol{\tau}_1 \quad \boldsymbol{\tau}_2)(0 \quad \mathbf{G}\cdot\boldsymbol{\tau}_1 \quad \mathbf{G}\cdot\boldsymbol{\tau}_2)^T. \tag{2.13}$$

Next, in the normal direction, taking the inner product of Eq. (2.7) with $\mathbf{n}$ gives

$$\begin{aligned}[p_d] &= -2\,[\mu]\,(\mathbf{n}\cdot\nabla\mathbf{u}\cdot\mathbf{n}) - \mathbf{G}\cdot\mathbf{n} \\ &= \gamma\kappa - [\rho]_\Gamma\,\mathbf{g}\cdot\mathbf{x} - 2\,[\mu]\,(\mathbf{n}\cdot\nabla\mathbf{u}\cdot\mathbf{n})\,,\end{aligned} \tag{2.14}$$

which describes the normal pressure discontinuity across the interface.

2.3. *Discretization of the viscosity jump*

Consider a case where the interface is located between two nodes i and $i+1$. Without loss of generality, let us assume that the phase indicator ϕ satisfies $\phi_i > 0.5$ ($\mathbf{x}_i \in \Omega_+$) and $\phi_{i+1} < 0.5$ ($\mathbf{x}_{i+1} \in \Omega_-$). If we define an auxiliary variable

$$\theta = \frac{|\phi_i|}{|\phi_i| + |\phi_{i+1}|}, \tag{2.15}$$

then the interface location can be represented as

$$\mathbf{x}_\Gamma = \mathbf{x}_i + \theta(\mathbf{x}_{i+1} - \mathbf{x}_i) = \mathbf{x}_i + \theta\Delta x. \tag{2.16}$$

Recalling the general equation for the pressure jump due to viscosity discontinuity from Eq. (2.10), we introduce $\mathbf{J}$ as

$$[\mu\nabla\mathbf{u}] = \mathbf{J}, \tag{2.17}$$

noting that $\mathbf{J}$ is spatially continuous and smooth (Kang *et al.* 2000). The jump condition at the interface can then be expressed as a linear interpolation

$$J_\Gamma = (1-\theta)J_i + \theta J_{i+1}. \tag{2.18}$$

Using this, the viscosity jump can be discretized as

$$\mu_{i+1}\frac{\mathbf{u}_{i+1} - \mathbf{u}_\Gamma}{(1-\theta)\Delta x} - \mu_i\frac{\mathbf{u}_\Gamma - \mathbf{u}_i}{\theta\Delta x} = J_\Gamma. \tag{2.19}$$

Solving for $\mathbf{u}_\Gamma$ and substituting into the viscous contribution at node $i+1$ yields

$$(\mu\mathbf{u}_x)_{i+1} = \mu_{i+1}\frac{\mathbf{u}_{i+1} - \mathbf{u}_\Gamma}{(1-\theta)\Delta x} = \hat{\mu}\frac{\mathbf{u}_{i+1} - \mathbf{u}_i}{\Delta x} + \frac{\hat{\mu}J_\Gamma\theta}{\mu_i}, \tag{2.20}$$

where the effective viscosity $\hat{\mu}$ is

$$\hat{\mu} = \frac{\mu_i\mu_{i+1}}{(1-\theta)\mu_i + \theta\mu_{i+1}}. \tag{2.21}$$

The jump $\mathbf{J}$ can be computed from Eq. (2.10), equivalent to Eq. (30) in Kang *et al.* (2000). For further details, readers are referred to Liu *et al.* (2000).

In fact, there are several different ways to discretize the viscous term. From

$$\nabla\cdot(2\mu\mathbf{D}) = \mu\nabla\cdot(2\mathbf{D}) + 2\mathbf{D}\cdot\nabla\mu, \tag{2.22}$$

it is evident that the viscous jump is already accounted for when computing the divergence of the full viscous term. Sussman *et al.* (2007) discretized the left-hand side, while Kang *et al.* (2000) applied the right-hand side combined with Eq. (2.10). Lalanne *et al.* (2015) suggested a simplified form with

$$\nabla\cdot(2\mu\mathbf{D}) = \nabla\cdot\left[\mu\left(\nabla\mathbf{u} + (\nabla\mathbf{u})^{\mathrm{T}}\right)\right] = \mu\nabla^2\mathbf{u} + \nabla\mu\cdot\nabla\mathbf{u}^T, \tag{2.23}$$

where the first term is used in the predictor step and the second in the Poisson equation to account for the pressure jump. Although this yields satisfactory results, it is less

accurate than the other two approaches. Other studies, such as Vukčević *et al.* (2017) and Haghshenas *et al.* (2019), integrate density within the divergence, applying the jump condition on kinematic viscosity. While acceptable in some test cases (Peltonen *et al.* 2020), this can lead to deviations in shear-layer tests. Interestingly, Peltonen *et al.* (2020) also showed that omitting the viscous term in the pressure jump has negligible effect. For flows in which the viscous contribution is expected to be small, Desjardins *et al.* (2008) employed a viscosity model for mixture cells given by $\mu = \phi_1\mu_1 + (1-\phi_1)\mu_2$.

Special care is required when discretizing the viscous term. In this work, we follow Sussman *et al.* (2007), retaining all contributions from the viscosity jump, even if their effect is small. This discretization of viscosity is intimately connected to the pressure solver.

2.4. *Discretization of the pressure jump*

The connection between the jump condition and the source term in the Poisson equation was detailed by Lalanne *et al.* (2015). Consider the Laplace equation

$$\Delta\psi = 0. \tag{2.24}$$

Given a jump condition at the interface

$$[\psi]_\Gamma = a(\mathbf{x}_\Gamma), \tag{2.25}$$

it can be shown that

$$\iiint_\Omega \nabla\psi \mathrm{d}\Omega = \iiint_\Omega a(\mathbf{x}_\Gamma)\mathbf{n}\delta_\Gamma \mathrm{d}\Omega; \tag{2.26}$$

adding a source term on the right-hand side of the Poisson equation enforces the jump condition at the boundary.

To compute the source term for the Poisson equation, we follow the derivation presented in Desjardins *et al.* (2008). For a variable ζ, the jump across the interface Γ is defined as $[\zeta]_\Gamma$. The GFM assumes that the jumps of ζ and its derivatives, $[\partial\zeta/\partial\mathbf{x}]_\Gamma$, are known at the interface. The GFM extends ζ continuously from each phase, allowing the definition of jumps not only at the interface but also in its neighborhood. A Taylor series expansion around the interface gives

$$[\zeta] = [\zeta]_\Gamma + (x - x_\Gamma)\left[\frac{\partial\zeta}{\partial\mathbf{x}}\right]_\Gamma + \frac{1}{2}(x-x_\Gamma)^2\left[\frac{\partial^2\zeta}{\partial\mathbf{x}^2}\right]_\Gamma + O((x-x_\Gamma)^3). \tag{2.27}$$

The derivative at a ghost node is approximated as

$$\left.\frac{\partial\zeta}{\partial x}\right|_{g,i} = \frac{\zeta_{g,i+1} - \zeta_{g,i-1}}{2\Delta x} + O(\Delta x^2) = \frac{\zeta_{l,i+1} - [\zeta]_{i+1} - \zeta_{g,i-1}}{2\Delta x} + O(\Delta x^2), \tag{2.28}$$

with

$$[\zeta]_{i+1} = [\zeta]_\Gamma + (x_{i+1} - x_\Gamma)\left[\frac{\partial\zeta}{\partial\mathbf{x}}\right]_\Gamma + O((x_{i+1}-x_\Gamma)^2). \tag{2.29}$$

Applying this to the Laplacian of the pressure

$$\frac{\partial}{\partial x}\left(\frac{1}{\rho}\frac{\partial p}{\partial x}\right) = \frac{1}{\rho_g}\frac{p_{g,i+1} - 2p_{g,i} + p_{g,i-1}}{\Delta x^2} + O(\Delta x^2) \tag{2.30}$$

$$= \frac{1}{\rho_g}\frac{p_{l,i+1} - [p]_{i+1} - 2p_{g,i} + p_{g,i-1}}{\Delta x^2} + O(\Delta x^2), \tag{2.31}$$

where

$$[p]_{i+1} = [p]_\Gamma + (x_{i+1} - x_\Gamma)\left[\frac{\partial p}{\partial \mathbf{x}}\right]_\Gamma + O((x_{i+1} - x_\Gamma)^2). \tag{2.32}$$

If velocity is continuous across the interface,

$$\left[\frac{1}{\rho}\frac{\partial p}{\partial x}\right]_\Gamma = 0. \tag{2.33}$$

Using

$$[AB] = \hat{B}[A] + \hat{A}[B], \quad \hat{A} = aA_R + bA_L,\ \hat{B} = bB_R + aB_L,\ a + b = 1, \tag{2.34}$$

we obtain

$$\left[\frac{\partial p}{\partial x}\right]_\Gamma = -\rho_l \left[\frac{1}{\rho}\right] \left.\frac{\partial p}{\partial x}\right|_{g,\Gamma} = -\rho_g \left[\frac{1}{\rho}\right] \left.\frac{\partial p}{\partial x}\right|_{l,\Gamma}. \tag{2.35}$$

Approximating

$$\left.\frac{\partial p}{\partial x}\right|_{g,\Gamma} = \left.\frac{\partial p}{\partial x}\right|_{g,i+1/2} + O(x_{i+1/2} - x_\Gamma), \tag{2.36}$$

the pressure jump at $i+1$ is obtained via inversion,

$$[p]_{i+1} \approx [p]_\Gamma - (x_{i+1} - x_\Gamma)\rho_l \left[\frac{1}{\rho}\right] \left.\frac{\partial p}{\partial x}\right|_{g,i+1/2} \tag{2.37}$$

$$= [p]_\Gamma - (x_{i+1} - x_\Gamma)\rho_l \left[\frac{1}{\rho}\right] \frac{p_{g,i+1} - p_{g,i}}{\Delta x} \tag{2.38}$$

$$= [p]_\Gamma - (x_{i+1} - x_\Gamma)\rho_l \left[\frac{1}{\rho}\right] \frac{p_{l,i+1} - [p]_{i+1} - p_{g,i}}{\Delta x}. \tag{2.39}$$

Introducing the subcell interface location $\theta = (x_\Gamma - x_i)/\Delta x$ and a modified density

$$\rho^* = \rho_g\theta + \rho_l(1-\theta), \tag{2.40}$$

the pressure jump at x_{i+1} becomes

$$[p]_{i+1} = \frac{\rho_g}{\rho^*}[p]_\Gamma + \left(1 - \frac{\rho_g}{\rho^*}\right)(p_{l,i+1} - p_{g,i}). \tag{2.41}$$

Finally, the discretized Laplacian of the pressure at node i is

$$\left.\frac{\partial}{\partial x}\left(\frac{1}{\rho}\frac{\partial p}{\partial x}\right)\right|_{g,i} = \frac{1}{\Delta x^2}\left\{\frac{1}{\rho^*}(p_{l,i+1} - p_{g,i}) - \frac{1}{\rho^*}(p_{l,i+1} - p_{g,i}) - [p]_\Gamma\right\}. \tag{2.42}$$

This formulation ensures that the surface tension force is directly embedded in the pressure gradient, preserving the discrete balance between pressure and surface tension.

2.5. *Solution procedure*

Having described the discretization of viscosity and pressure jumps at the interface, we now summarize the procedure used to solve the governing equations. The final form of the momentum equation solved in this study is

$$\frac{\partial \mathbf{u}}{\partial t} + \mathbf{u}\cdot\nabla\mathbf{u} - \frac{1}{\rho}\nabla\cdot\left[\mu\left(\nabla\mathbf{u} + (\nabla\mathbf{u})^{\mathrm{T}}\right)\right] = -\frac{\nabla p_d}{\rho}, \tag{2.43}$$

subject to the interfacial jump condition

$$[p_d]_\Gamma = \gamma\kappa - [\rho]_\Gamma\,\mathbf{g}\cdot\mathbf{x}, \tag{2.44}$$

where the contributions from viscosity and pressure jumps, as detailed in the previous subsections, are fully incorporated. The solution procedure is based on the PISO method. Integrating Eq. (2.43) over a control volume leads to the intermediate velocity equation

$$A_p \mathbf{u}_p^* + H(\mathbf{u}_N) = -\frac{\nabla p_d^n}{\rho}, \tag{2.45}$$

where A_p and $H(\mathbf{u}_N)$ are the diagonal and off-diagonal coefficients corresponding to the central cell p and its neighboring cells N, respectively. The viscous term, discretized with the interface-aware formulation described earlier, is included in $H(\mathbf{u}_N)$. The intermediate velocity $\mathbf{u}^*$ is then corrected by solving the pressure Poisson equation with the embedded jump conditions for

$$\nabla \cdot \left(A_p^{-1} \frac{\nabla p_d}{\rho} \right) = \nabla \cdot \left(A_p^{-1} H(\mathbf{u}_N) \right) + \nabla \cdot \left\{ \frac{1}{\rho} \Big(\gamma \kappa_\Gamma - [\rho]_\Gamma \, \mathbf{g} \cdot \mathbf{x}_\Gamma \Big) \mathbf{n} \delta_\Gamma \right\}. \tag{2.46}$$

Finally, the corrected cell-center velocity is reconstructed as

$$\mathbf{u}^{n+1} = A_p^{-1} \left\{ H(\mathbf{u}_N^*) - \frac{1}{\rho} \Big(\nabla p_d - \big(\gamma \kappa \Gamma - [\rho]_\Gamma \, \mathbf{g} \cdot \mathbf{x}_\Gamma \big) \mathbf{n} \delta_\Gamma \Big) \right\}. \tag{2.47}$$

This procedure ensures that the effects of viscosity jumps, pressure discontinuities, and surface tension are consistently incorporated into the velocity update.

2.6. *Clarification on surface tension force discretization*

For comparison with the current approach, widely adopted interface-capturing methods, namely the algebraic VOF method by Higuera (2015), the geometric VOF method by Roenby *et al.* (2016), and the algebraic VOF method combined with the reconstructed distance function (RDF) approach by Scheufler & Roenby (2019), are introduced. We provide a clear distinction between these schemes in terms of surface tension force discretization.

Numerical approximations of surface tension, obtained by coupling volumetric fields with the surface geometry, are critical within the finite-volume framework. For an elementary control volume Ω, the volumetric formulation of the surface tension force acting on Ω can be expressed by a numerical approximation of the surface Dirac function as follows (Peskin 1977),

$$\int_\Omega f_\sigma = \int_\Omega \sigma \kappa \mathbf{n} \delta_s. \tag{2.48}$$

Using a numerical approximation for the Heaviside function, H, the integrand in Eq. (2.48) is approximated as

$$\sigma \kappa \mathbf{n} \delta_s = \sigma \kappa \nabla H(\mathbf{x} - \mathbf{x}_\Gamma). \tag{2.49}$$

The compared CSF method assumes that the Heaviside function corresponds to the volume fraction field ϕ (cf. Sussman *et al.* (1994), who approximated H as a smooth function). The geometric VOF and algebraic VOF approaches used in this study fall into the same category. We emphasize that the GFM also belongs to this category (Eqs. (2.48)–(2.49)) for surface tension discretization, with the Heaviside function defined as unity inside the interface and zero otherwise (Popinet 2018). Consequently, the surface Dirac function is necessarily limited to a characteristic interface thickness on the order of the grid size. This should not be confused with the sharp-Heaviside approximation; although the Heaviside function is sharp, it is insensitive within the characteristic interface thickness.

When described as sharp, the sharp-interface representation indicates that no mixed-cell representation exists when using the sharp Heaviside function. Readers are referred to Popinet (2018) for a comprehensive overview of surface tension discretization.

2.7. *Well-balanced method*

All approaches used in this study employ a well-balanced algorithm, in which the gradient of the pressure is discretized in the same manner as the volume fraction. However, they differ in the method used to calculate curvature at the interface location.

The estimate of the interface normal, $\mathbf{n}\delta_s$, in the compared CSF approaches by (Higuera 2015) and Roenby *et al.* (2016), remains coupled with the curvature estimate, κ. In contrast, the current GFM implementation decouples this relationship by using the height function to compute curvature, which is evaluated at the interpolated interface location (Francois *et al.* 2006; Abadie *et al.* 2015). Similarly, the algebraic VOF method with RDF also decouples the normal and curvature estimations by employing the RDF.

3. Results and discussion

A series of canonical test cases is presented to evaluate the accuracy and robustness of the present method in comparison with the approaches introduced above. The selected benchmarks include a static drop (or bubble), a damped surface wave, and a two-phase shear layer.

3.1. *Static drop*

A static drop of radius $R = 0.4$ m is placed at the center of a square domain $[-1, 1]$ m $\times[-1, 1]$ m. The surface tension coefficient is set to $\gamma = 1.0$ N/m. The flow field is initialized at rest, and slip boundary conditions are applied at the domain boundaries. To ensure the system reaches equilibrium, the simulation is advanced for 10,000 time steps with a fixed time step size of $\Delta t = 0.0001$ s.

From this configuration, the exact pressure jump and curvature across the interface are known to be $p_{\text{exact}} = 2.5$ Pa and $\kappa_{\text{exact}} = 2.5$ m^{-1}, respectively. The curvature and pressure errors are defined as

$$\mathcal{E}_\kappa = \frac{\kappa - \kappa_{\text{exact}}}{\kappa_{\text{exact}}}, \qquad \mathcal{E}_p = \frac{p - p_{\text{exact}}}{p_{\text{exact}}}, \tag{3.1}$$

and are evaluated for grid resolutions of $N_x = 125, 162, 208, 269, 348, 449$, and 580.

Figure 1 shows the pressure field for a grid spacing of $\Delta x = 0.016$ m. The color map reveals two distinct pressure levels inside and outside the drop, corresponding to $p_{\text{in}} = 2.5019$ Pa and $p_{\text{out}} = -2.073 \times 10^{-6}$ Pa, indicating the absence of mixed cells and thus a sharply resolved interface.

The error metrics from Eq. (3.1) are evaluated for all resolutions, and the results are shown in Figure 2. The curvature error of the present method decreases proportionally to Δx^{-2}, while those from conventional interface-capturing methods increase roughly with Δx^{1} (Cummins *et al.* 2005). Consequently, the pressure error, which arises from the balance between the pressure gradient and surface tension, follows the same scaling trend, which is a second-order decay for the present method and a first-order growth for the others.

These results imply that the present sharp-interface formulation generates spurious currents of significantly smaller magnitude as the grid is refined. This property becomes

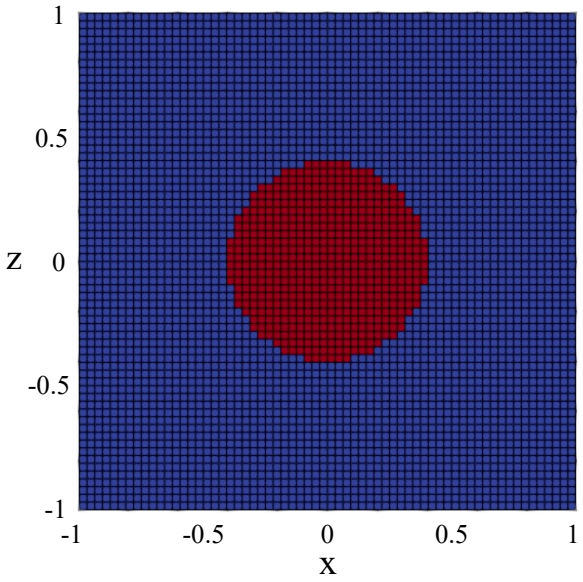

Figure 1: Pressure field of a static drop with grid resolution $\Delta x = 0.016$ m. The absence of mixed cells indicates a sharply captured pressure discontinuity across the interface.

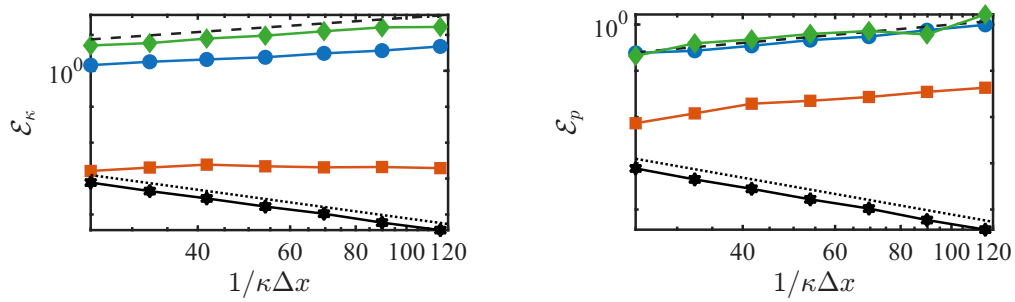

(a) (b)

Figure 2: (a) Curvature error and (b) pressure error scaling as a function of grid resolution. Symbols represent the geometric VOF method (blue circles), the algebraic VOF method (red squares), the geometric VOF with RDF method (green diamonds), and present method (black hexagrams). Black dashed and dotted lines indicate slope $+1$ and -2, respectively.

critical when resolving small-scale structures near the interface, where numerical artifacts could otherwise contaminate the physically relevant dynamics.

3.2. *Damped surface wave*

The damped surface wave test follows the setup described by Hwang & Jain (2024). To isolate the influence of surface tension and viscous damping, a unity density ratio ($\rho_1 = \rho_2$) is considered. Simulations are performed with grid spacings $\Delta x = 2\pi/16$,

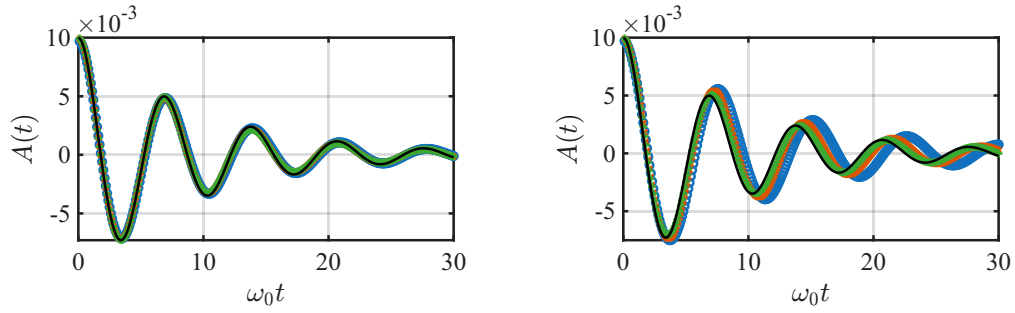

Figure 3: Temporal evolution of the damped surface wave amplitude for (a) the present method and (b) the algebraic VOF method. Symbols denote grid resolutions $\Delta x = 2\pi/16$ (blue circles), $2\pi/32$ (red crosses), and $2\pi/64$ (green plus signs). The black solid line indicates the analytical solution.

$2\pi/32$, and $2\pi/64$. The amplitude decay over time is shown in Figure 3 for both the present method and an algebraic VOF scheme.

The present method shows excellent agreement with the analytical solution even at the coarsest resolution, whereas the algebraic VOF method deviates noticeably, failing to converge even at the finest grid. The initial amplitude $A(t_0) = 0.01 \times 2\pi$ is already smaller than a single grid cell, yet the present method captures its decay accurately. This demonstrates that the accurate curvature evaluation using height functions and subcell-resolved interface reconstruction provides a clear advantage in tracking subgrid-scale interfacial motion.

3.3. *Two-phase shear layer*

The final test case considers a two-phase shear layer, for which an analytical similarity solution exists,

$$\frac{\partial u}{\partial t} = \nu_i \frac{\partial^2 u}{\partial y^2}. \tag{3.2}$$

The interface is located at $y = 2$ m within a vertical domain $y \in [0, 4]$ m. The analytical solution is expressed as

$$u(y,t) = \begin{cases} A + (u_2 - A)\,\mathrm{erf}\left(\dfrac{2-y}{2\sqrt{\nu_2 t}}\right), & 0 \le y < 2, \\ A + (u_1 - A)\,\mathrm{erf}\left(\dfrac{y-4}{2\sqrt{\nu_2 t}}\right), & 2 \le y < 4, \end{cases} \tag{3.3}$$

where

$$A = \frac{\mu_1 \dfrac{u_1}{\sqrt{\nu_1}} + \mu_2 \dfrac{u_2}{\sqrt{\nu_2}}}{\dfrac{u_1}{\sqrt{\nu_1}} + \dfrac{u_2}{\sqrt{\nu_2}}}. \tag{3.4}$$

Two fluids with properties corresponding to air (bottom) and water (top) are initialized with $u_{\mathrm{air}} = 10$ m/s and $u_{\mathrm{water}} = 1$ m/s. The simulation is advanced to $t = 5000$ s, and the evolution of the velocity field is compared with the analytical solution in Figure 4.

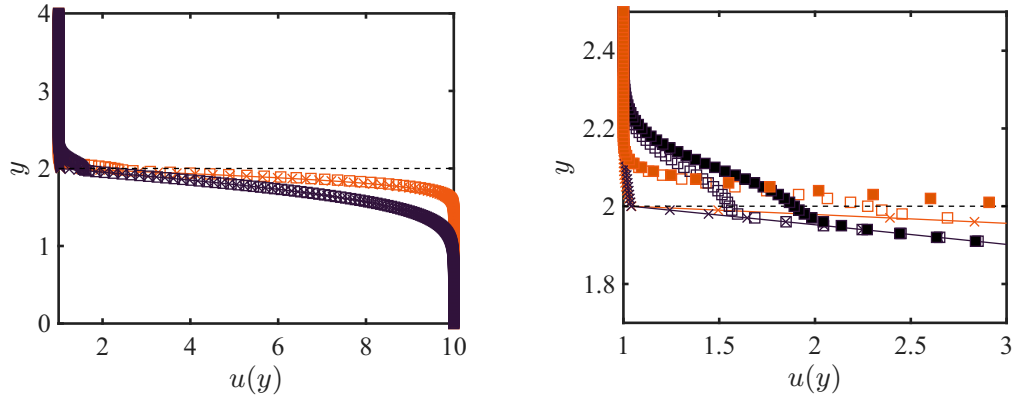

(a) (b)

Figure 4: Temporal evolution of the velocity profile in the two-phase shear layer: (a) full domain and (b) magnified view near the interface. Colors indicate different time instants at $t = 0$ (red) and $t = 5000$ s (black). Symbols denote the present method (crosses) and the algebraic VOF method (squares). In (b), results for a twice thicker diffuse interface are also shown as solid symbols. The solid lines indicate the analytical solution.

For reference, an additional simulation using a diffuse interface of twice the nominal thickness is included.

Both the present and algebraic VOF methods capture the general evolution of the shear layer, with the velocity on the lighter (air) side converging rapidly to the analytical profile. However, near the interface, the algebraic VOF solution deviates by more than 50% from the analytical velocity in the heavier (water) phase, whereas the present method accurately reproduces the sharp transition. Increasing the interface thickness further degrades the accuracy on the heavy side, highlighting the sensitivity to interface resolution. This finding suggests that the sharp-interface formulation is particularly advantageous in high-shear, long-duration simulations where interfacial fidelity is critical.

4. Conclusions

We revisit the GFM for incorporating interfacial physics in multiphase flow simulations. Through a series of canonical test cases, we assessed and compared the potential of the GFM to resolve small-scale flow structures near the interface on both sides. When coupled with the height function, the static drop case demonstrated that the curvature error decreases with grid refinement, leading to an accurate prediction of the pressure jump across the interface. This result indicates that the present approach generates significantly smaller spurious currents, which is advantageous when refining the grid near interfaces to capture small-scale flow dynamics.

Owing to its sharp interface representation, the present method eliminates the ambiguity associated with mixed cells, an issue common in approaches with finite interface thickness, where cell-averaged properties are influenced by artificial compression terms and background phase indicators. Furthermore, in the damped surface wave case, the present method outperformed approaches based on the compared CSF approach, showing excellent agreement with the analytical solution even at the coarsest resolution. This

outcome underscores the robustness of directly discretizing jump conditions when modeling moving interfaces.

Finally, the two-phase shear layer test demonstrated that the present method remains insensitive to interface thickness, which otherwise deteriorates velocity predictions on the heavier fluid side.

In summary, the results suggest that for flows involving strong shear near interfaces, sharp-interface approaches such as the GFM coupled with the height function can offer clear advantages in accuracy and stability. Nevertheless, further investigation is required for complex cases with large density and viscosity ratios to more comprehensively understand the method's applicability and limitations.

Acknowledgments

The author gratefully recognizes support from the National Science Foundation under Grant No. 2131961. This material is based upon work supported by the Department of Energy, National Nuclear Security Administration under Award Number DE-NA0003968. The author also acknowledges Dr. Alexander N. W. Cicchino of the Center for Turbulence Research for helpful comments and discussions.

REFERENCES

Abadie, T., Aubin, J. & Legendre, D. 2015 On the combined effects of surface tension force calculation and interface advection on spurious currents within volume of fluid and level set frameworks. *J. Comput. Phys.* **297**, 611–636.

Bo, W. & Grove, J. W. 2014 A volume of fluid method based ghost fluid method for compressible multi-fluid flows. *Comput. Fluids* **90**, 113–122.

Brackbill, J. U., Kothe, D. B. & Zemach, C. 1992 A continuum method for modeling surface tension. *J. Comput. Phys.* **100**, 335–354.

Cho, H. & Kang, M. 2021 Fully implicit and accurate treatment of jump conditions for two-phase incompressible Navier–Stokes equations. *J. Comput. Phys.* **445**, 110587.

Cummins, S. J., Francois, M. M. & Kothe, D. B. 2005 Estimating curvature from volume fractions. *Computers & Structures* **83**, 425–434.

Desjardins, O., Moureau, V. & Pitsch, H. 2008 An accurate conservative level set/ghost fluid method for simulating turbulent atomization. *J. Comput. Phys.* **227**, 8395–8416.

Fedkiw, R. P., Aslam, T., Merriman, B. & Osher, S. 1999 A non-oscillatory Eulerian approach to interfaces in multimaterial flows (the ghost fluid method). *J. Comput. Phys.* **152**, 457–492.

Francois, M. M., Cummins, S. J., Dendy, E. D., Kothe, D. B., Sicilian, J. M., & Williams, M. W. 2006 A balanced-force algorithm for continuous and sharp interfacial surface tension models within a volume tracking framework. *J. Comput. Phys.* **213**, 141–173.

Haghshenas, M., Wilson, J. A. & Kumar, R. 2019 Finite volume ghost fluid method implementation of interfacial forces in PISO loop. *J. Comput. Phys.* **376**, 20–27.

Higuera, P. 2015 Application of computational fluid dynamics to wave action on structures. *PhD thesis, Universidade de Cantabria*.

Hwang, H. & Jain, S. S. 2024 A robust phase-field method for two-phase flows on unstructured grids. *J. Comput. Phys.* **507**, 112972.

Kang, M., Fedkiw, R. P. & Liu, X. 2000 A boundary condition capturing method for multiphase incompressible flow. *J. Sci. Comput.* **15**, 323–360.

Lalanne, B., Villegas, L. R., Tanguy, S. & Risso, F. 2015 On the computation of viscous terms for incompressible two-phase flows with level set/ghost fluid method. *J. Comput. Phys.* **301**, 289–307.

Liu, X., Fedkiw, R. P. & Kang, M. 2000 A boundary condition capturing method for Poisson's equation on irregular domains. *J. Comput. Phys.* **160**, 151–178.

Peltonen, P., Kanninen, P., Laurila, E. & Vuorinen, V. 2020 The ghost fluid method for OpenFOAM: a comparative study in marine context. *Ocean Eng.* **216**, 108007.

Peskin, C. S. 1977 Numerical analysis of blood flow in the heart. *J. Comput. Phys.* **25**, 220–252.

Roenby, J., Bredmose, H. & Jasak, H. 2016 A computational method for sharp interface advection. *R. Soc. Open Sci.* **3**, 160405.

Popinet, S. 2018 Numerical models of surface tension. *Annu. Rev. Fluid Mech.* **50**, 49–75.

Scheufler, H. & Roenby, J. 2019 Accurate and efficient surface reconstruction from volume fraction data on general meshes. *J. Comput. Phys.* **383**, 1–23.

Sussman, M., Smereka, P. & Osher, S. 1994 A level set approach for computing solutions to incompressible two-phase flow. *J. Comput. Phys.* **114**, 146–159.

Sussman, M., Smith, K. M., Hussaini, M. Y., Ohta, M. & Zhi-Wei, R. 2007 A sharp interface method for incompressible two-phase flows. *J. Comput. Phys.* **221**, 469–505.

Vukčević, V., Jasak, H. & Gatin, I. 2017 Implementation of the ghost fluid method for free surface flows in polyhedral finite volume framework. *Comput. Fluids* **153**, 1–19.